Drag and non-drag force influences in numerical simulations of metallurgical ladles

Carlos G. Méndez*, Norberto Nigro, Alberto Cardona

CIMEC (INTEC), UNL-Conicet, Güemes 3450, 3000 Santa Fe, Argentina

Abstract

The modeling of metallurgical gas stirred ladles involves the interaction between several different phases with effects that, in many cases, have been considered in the literature. However, the way in which the different non-drag effects influence the behavior of this system is not clear. In this paper we analyze how numerical results are affected when the parameters used in modeling non-drag forces (such as virtual mass, lift, and turbulent dispersion force) are varied. Other effects such as the increment in turbulence due to the bubbles, a deformable free surface, and the influence of the bubble size were also considered. The knowledge of the way in which each physical phenomenon modifies the behavior of the main variables of the system allowed the fitting of experimental data in a variety of conditions. We conclude that a gas stirred ladle can be properly represented when the non-drag effects analyzed here are included, and give suitable values for the different parameters considered.
© 2004 Elsevier B.V. All rights reserved.

Keywords: Multiphase flow; Stirred ladle; Non-drag forces

1. Introduction

From the industrial point of view, knowledge of flow conditions in a metallurgical ladle is of fundamental importance for the optimization of the refining process. Three different phases coexist in the refining operations in a metallurgical ladle: the molten metal, the slag and the argon injected to induce stirring. The dispersed gas phase induces a recirculating flow in the metal and generates turbulence in the argon plume region. As a consequence of buoyancy, the slag has a tendency to stratify above the metal, but there is also entrainment caused by the metal flow. Knowledge of the flow conditions of the metal, particularly in the region where it is in contact with the slag, helps in the comprehension of various phenomena such as mixing, slag emulsification, and chemical reactions between phases.

A water–air downscaled physical model is frequently used to simulate the metal and the argon, whereas the slag is modeled using oil or kerosene to avoid difficulties due to extreme operating conditions of the metal–argon system [1]. In this work, the numerical simulation of the former model was initially investigated, in order to keep the model as simple as possible and to compare results with the large amount of experimental data already existing for water–air systems. In particular, the experimental dataset obtained by Castillejos and Brimacombe [2] was used in this paper. In addition to that, the way the principal characteristics of the flow are modified when the free surface and the slag are incorporated into the model is shown. The results compare very well to experimental measurements, which suggests that the effects included in the model are the most relevant ones in order to suitably represent the ladle conditions.

Numerical simulations are based on the solution of the Navier–Stokes equations for a multi-phase turbulent flow. The way in which the gas is dispersed in the ladle is governed by the buoyant force and by the interaction with the liquid phase. Interaction between phases is due mainly to the drag force. However, not only the drag force but also non-drag forces (such as the virtual mass force, the lift force, and the turbulent dispersion force) are important and have to be considered. If the interest is not only in determining the ve-

* Corresponding author.
  E-mail address: cgmendez@ceride.gov.ar (C.G. Méndez).

locity field of the liquid phase, but also the gas velocity and volume fraction, non-drag forces have to be considered. Having a good estimation of the volume fraction of the dispersed phases will be of utmost importance in the description of the slag emulsification phenomena.

2. Balance equations

Since the mail objective is to obtain rather global information about gas phase, e.g. bubble velocity and concentration, and not to study how a bubble is deformed, and as the length scale to solve is larger than the scale in which phases are mixed, an Eulerian–Eulerian approach was chosen to describe the system. Each phase in this formulation is treated as an interpenetrating continuum, i.e., each phase is assumed present in each control volume, and a volume fraction equal to the occupied fraction of the control volume is assigned.

Large bubbles can have a velocity field different from that of the continuous phase. In this case, each phase has its own movement equation, and the interaction between phases has to be modeled. This is the regime of current interest, and it is best described by the so-called multi-fluid model. In this model, a separate solution field exists for each phase, and transported quantities interact via inter-phase transfer terms. Phases may have different velocities, but tend to equalize because of inter-phase forces. Therefore, balance equations consist of equations corresponding to separate one-phase systems plus some additional terms that take into account their interaction.

The phases are labeled here by Greek indices α, β, γ, ..., and the number of phases is denoted by N_P and the volume fraction of each phase by r_α. The balance equations in the incompressible case are [3]

$$\frac{\partial r_\alpha}{\partial t} + \nabla \cdot (r_\alpha \boldsymbol{U}_\alpha) = 0, \tag{1}$$

$$\rho_\alpha \frac{\partial (r_\alpha \boldsymbol{U}_\alpha)}{\partial t} + \rho_\alpha \nabla \cdot (r_\alpha \boldsymbol{U}_\alpha \boldsymbol{U}_\alpha)$$
$$- \nabla \cdot (r_\alpha \mu_\alpha (\nabla \boldsymbol{U}_\alpha + (\nabla \boldsymbol{U}_\alpha)^{\mathrm{T}}))$$
$$= r_\alpha (\boldsymbol{B}_\alpha - \nabla p_\alpha) + \sum_{\beta=1}^{N_P} c_{\alpha\beta}^{(d)} (\boldsymbol{U}_\beta - \boldsymbol{U}_\alpha) + \boldsymbol{F}_\alpha, \tag{2}$$

$$\sum_{\alpha=1}^{N_P} r_\alpha = 1, \tag{3}$$

$$p_\alpha = p_1 = p, \quad 2 \le \alpha \le N_P, \tag{4}$$

where $\boldsymbol{U}$ denotes velocity; ρ, density; μ, viscosity; $\boldsymbol{B}$, body forces; p, pressure; and superscript T the transpose of the tensor. Terms containing coefficients $c_{\alpha\beta}^{(d)}$ are the inter-phase drag forces, and the terms $\boldsymbol{F}_\alpha$ are any other inter-phase non-drag forces.

3. Turbulence in two-phase flow

The subject of multi-phase turbulence modeling is not as well developed as single-phase turbulence modeling. There is no "industrial standard" model like the single-phase k–ε model, which is known to perform reasonably well in engineering applications in a wide range of problems. Therefore, the model adopted is the simplest possible generalization of the single-phase k–ε model to the multi-phase situation, the only modification being the possible inclusion of Sato's model for bubble induced turbulence.

3.1. Multi-fluid k–ε model

In the simple unmodified multi-fluid k–ε model, individual phases can be declared as turbulent or laminar. It is assumed that the eddy viscosity hypothesis holds for each turbulent phase and therefore molecular and turbulent diffusion of momentum is governed by an effective viscosity

$$\mu_{\alpha\,\mathrm{eff}} = \mu_\alpha + \mu_{\mathrm{T}\alpha}, \tag{5}$$

where the turbulent viscosity term is

$$\mu_{\mathrm{T}\alpha} = C_\mu \rho_\alpha \frac{k_\alpha^2}{\varepsilon_\alpha}. \tag{6}$$

Thus, the equations for the turbulent incompressible case are

$$\frac{\partial r_\alpha}{\partial t} + \nabla \cdot (r_\alpha \boldsymbol{U}_\alpha) = 0, \tag{7}$$

$$\rho_\alpha \frac{\partial (r_\alpha \boldsymbol{U}_\alpha)}{\partial t} + \rho_\alpha \nabla \cdot (r_\alpha \boldsymbol{U}_\alpha \boldsymbol{U}_\alpha)$$
$$- \nabla \cdot (r_\alpha \mu_{\alpha\,\mathrm{eff}} (\nabla \boldsymbol{U}_\alpha + (\nabla \boldsymbol{U}_\alpha)^{\mathrm{T}}))$$
$$= r_\alpha (\boldsymbol{B}_\alpha - \nabla (p_\alpha + \tfrac{2}{3}\rho_\alpha k_\alpha))$$
$$+ \sum_{\beta=1}^{N_P} c_{\alpha\beta}^{(d)} (\boldsymbol{U}_\beta - \boldsymbol{U}_\alpha) + \boldsymbol{F}_\alpha, \tag{8}$$

$$\sum_{\alpha=1}^{N_P} r_\alpha = 1, \tag{9}$$

$$p_\alpha = p_1 = p, \quad 2 \le \alpha \le N_P, \tag{10}$$

together with the transport equations for k and ε, which are practically the same as those corresponding to the single-phase case,

$$\rho_\alpha \frac{\partial (r_\alpha k_\alpha)}{\partial t} + \rho_\alpha \boldsymbol{U}_\alpha \cdot \nabla (r_\alpha k_\alpha) - \nabla \cdot \left(\left(\mu + \frac{\mu_{\mathrm{T}\alpha}}{\sigma_k} \right) r_\alpha \nabla k_\alpha \right)$$
$$= r_\alpha (P_\alpha - \rho_\alpha \varepsilon_\alpha) + \sum_{\beta=1}^{N_P} c_{\alpha\beta}^{(k)} (k_\beta - k_\alpha), \tag{11}$$

and

$$\rho_\alpha \frac{\partial(r_\alpha \varepsilon_\alpha)}{\partial t} + \rho_\alpha \boldsymbol{U}_\alpha \cdot \nabla(r_\alpha \varepsilon_\alpha) - \nabla \cdot \left(\left(\mu + \frac{\mu_{T\alpha}}{\sigma_\varepsilon} \right) r_\alpha \nabla \varepsilon_\alpha \right)$$

$$= C_1 \frac{\varepsilon_\alpha}{k_\alpha} P_\alpha - C_2 \rho_\alpha \frac{\varepsilon_\alpha^2}{k_\alpha} + \sum_{\beta=1}^{N_P} c_{\alpha\beta}^{(\varepsilon)} (\varepsilon_\beta - \varepsilon_\alpha), \tag{12}$$

In these equations, the shear production P_α is given by

$$P_\alpha = \mu_{\text{eff}} \nabla \boldsymbol{U}_\alpha : (\nabla \boldsymbol{U}_\alpha + (\nabla \boldsymbol{U}_\alpha)^{\text{T}}), \tag{13}$$

where the symbol ':' indicates double contraction of the tensors, and assumed values for used constants are $C_\mu = 0.09$, $C_1 = 1.44$, $C_2 = 1.92$, $\sigma_k = 1.0$, $\sigma_\varepsilon = 1.22$, as is usual for this model [4].

The only difference between the multi-phase transport equations for k and ε with the single-phase case is the inclusion of the inter-phase terms $\sum_{\beta=1}^{N_P} c_{\alpha\beta}^{(k)}(k_\beta - k_\alpha)$ and $\sum_{\beta=1}^{N_P} c_{\alpha\beta}^{(\varepsilon)}(\varepsilon_\beta - \varepsilon_\alpha)$ which interchange k and ε between phases. However, since in this case the dispersed phase has lower density and smaller momentum compared to the continuous phase and is high diluted in nearly all the ladle, air is modeled as laminar and these interchange terms are neglected.

4. Numerical modeling

Numerical results were obtained solving a system with the following characteristics:

- Two dimensions with axial symmetry.
- Isothermal and incompressible flow.
- Liquid phase (water) continuum and turbulent (k–ε model).
- Gas phase (air) dispersed and laminar, and capable of passing through the free surface.
- Air density depends only on hydrostatic pressure.
- Each phase has its own set of variables (multi-fluid model).
- Drag as well as non-drag forces are included.
- Deformable free surface.
- Grids of 40×25, 80×50 and 160×100 rectangular elements.

Strictly speaking, the flow regime in this system is never steady, but after a short transient (~ 2 s), the plume is completely developed and a pseudo-steady regime is established. The mean quantities used to compare to simulations, were measured in this regime. To avoid numerical difficulties, it is convenient to emulate what happens experimentally. Thus, transient calculations were made starting with a zero-flow condition until the pseudo-steady regime was achieved. Although the regime is pseudo-stationary, some non-stationary characteristics can be captured if the grid is refined enough. However, mean quantities were stabilized and converged for a grid of 40×25 elements. Therefore, all the results presented here, obtained using the code CFX4.4 [5], correspond to this coarse grid.

The general convergence criterion adopted was the monitoring of the residuals of all variables, stopping the calculation when they stagnate indicating that the pseudo-steady regime has been reached. When this state is achieved, the mass source residual (the sum of the absolute values of the net mass fluxes in every cell) is typically below 10^{-4} kg/s.

Fig. 1 shows some of the effects considered in this work. The drag force (Fig. 1a) is originated by pressure and friction between phases and acts in the opposite direction to that of the movement. The non-drag forces considered here were the virtual mass force, the lift force, and the turbulent dispersion force. The virtual mass force (Fig. 1b) represents the force due to the inertia of a bubble, including the surrounding liquid, when the bubble is accelerated. The lift force (Fig. 1c) appears because a bubble moving in a linear shear flow has an unsymmetrical pressure distribution on its external boundary. Pressure is lower in the region of the largest relative velocity and therefore bubbles are driven into this region due to a lift force that acts perpendicular to the relative motion of the phases. When the typical size of the dispersed phase is in the order of the fluctuation length scale of the continuous phase, the effect of diffusion should be considered. In the laminar case, this situation appears only when the phases are mixed at molecular level, which is not the present case. However, when the flow regime is turbulent, fluctuations of the continuous phase may be comparable to the bubble size, and diffusion may be important. This effect is usually taken into account through a non-drag force called turbulent dispersion force (Fig. 1d), but other alternatives exist, and they will be further discussed. Another effect that has to be taken into account is the turbulence that can be generated behind the bubbles. This effect can transform a laminar flow into a turbulent one, or it can increase an existing turbulence in the continuous phase.

All the effects mentioned above are always present. However, the relative importance of each one depends on the size of the bubbles and on the degree of turbulence in the system. In the literature, the drag force is always included to describe the interaction between phases, but sometimes some or all of the non-drag effects are neglected [6–10]. If the interest is in determining the velocity field of the liquid phase, drastic approximations of this kind may be used. However, in order to properly describe the gas velocity and volume fraction, non-drag forces have to be considered.

Preliminary results, including non-drag effects, are shown first. These results correspond to one of the cases studied by Castillejos and Brimacombe [2] (all the experimental data shown in this paper correspond to this reference). After that, the way in which non-drag effects were implemented, as well as how the numerical results can be improved when the influence of each of these effects is considered, is described in more detail.

In Fig. 2, the air volume fraction and streak lines representing the water velocity field are shown. This case corresponds to a cylindrical ladle with internal diameter of 500 mm and height of water of 400 mm. The nozzle, with a diameter of
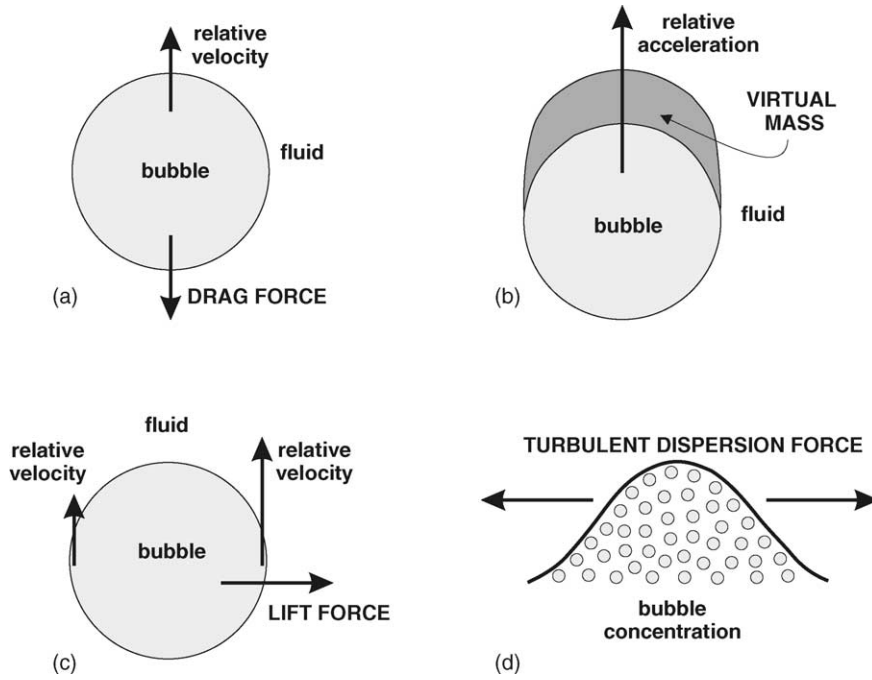
Fig. 1. Schematic representation of various effects considered in this work: (a) drag force, (b) virtual mass, (c) lift force and (d) turbulent dispersion force.
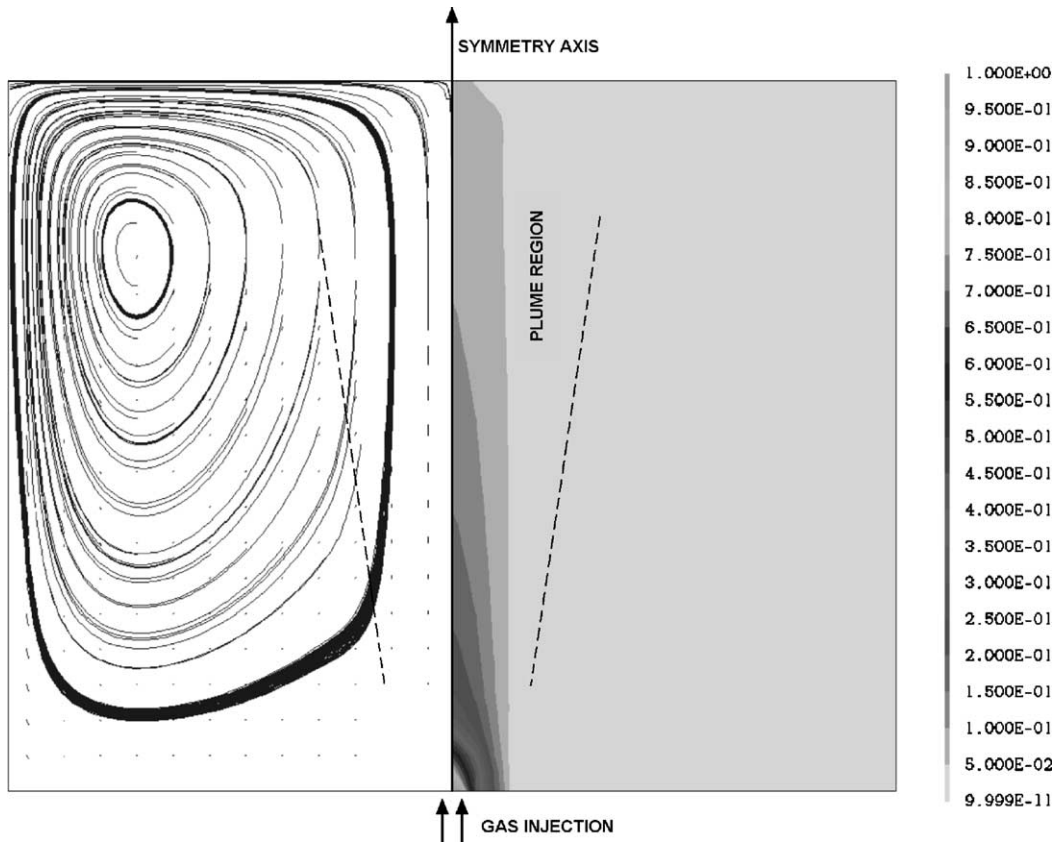

Fig. 2. Numerical result for the volume fraction of the air phase (right) and streak lines corresponding to the water phase (left).
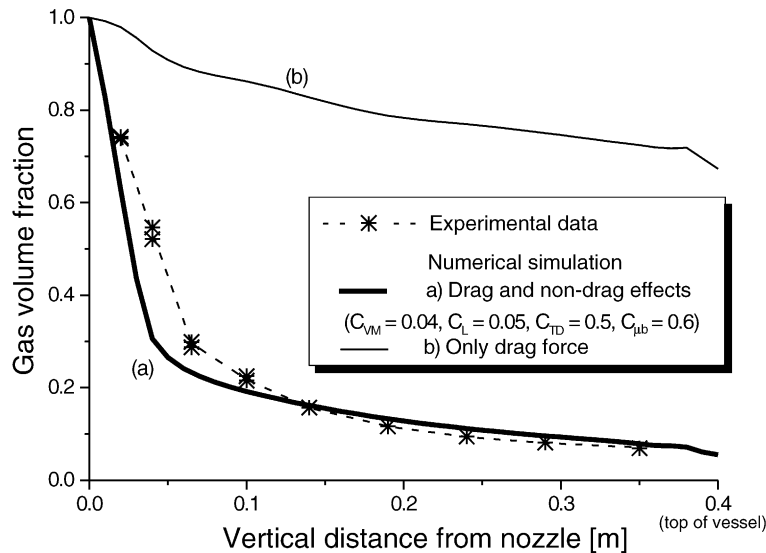
Fig. 3. Experimental [2] and numerical results for the volume fraction of the air phase on the symmetry axis of the ladle.

6.35 mm, was located at the center of the bottom of the ladle, and the gas flow rate was 371 cm³/s at STP (standard temperature and pressure). The way the air injected at the bottom of the ladle induces a recirculating flow in the water is seen in this figure.

The air volume fraction on the symmetry axis of the cylinder as a function of vertical distance from the nozzle is shown in Fig. 3, which also shows how the numerical predictions are modified when non-drag effects with typical coefficients are included.

Since the total gas flow rate integrated on any horizontal cross section is known and constant, the gas fraction distribution along the radial direction can be well described for engineering purposes provided its value at the symmetry axis ($r = 0$) is known. Lower gas volume fractions on the symmetry axis will correspond to more dispersed gas volume fractions in the radial direction. Therefore, the gas volume fraction distribution along the symmetry axis can be used as an indicator to see how well the dispersed phase distribution is being predicted. Results plotted on a linear scale seem to show good accordance between numerical predictions and experiments (Fig. 3). But when they are presented as in Fig. 4 on a log–log scale (in the same way they are plotted in Ref. [2]), the disagreement is evident even when non-drag effects are included.

One of the weak points in the numerical results is the difference with experiments near the nozzle. This region is hard to describe correctly because in this zone bubbles are large and breakup and coalescence phenomena are important. A good modeling of these phenomena requires the consideration of bubbles of different sizes, which is beyond the scope of this work.

The primary interest is not in the near-nozzle region but in the completely developed plume region where the bubble size

distribution is more stable. It has been observed experimentally [2] that far from the nozzle, gas volume fractions have a similar behavior for changing values of the gas flow rate, the nozzle diameter, and the bath depth. In a log–log graphic, the slope of the gas fraction curve is a feature of the system that is maintained in plumes with different characteristics (see, e.g., Fig. 5 of Ref. [2]), and it would be desirable to reproduce this feature in numerical simulations. As seen in Fig. 4, the main problem in the developed plume region is that the numerical and the experimental gas fraction curves have different slopes. The fact that even when working with a unique bubble size the gas fraction can be well described when the influence of the non-drag effects is taken into account will be shown below.
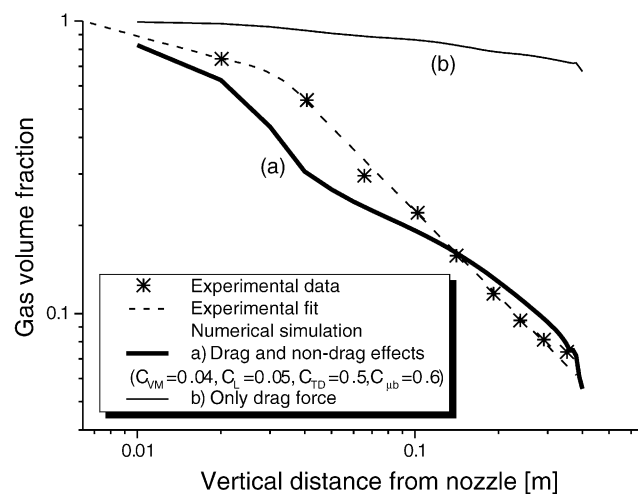

Fig. 4. Experimental [2] and numerical results for the volume fraction of the air phase on the symmetry axis of the ladle in a log–log graphic.
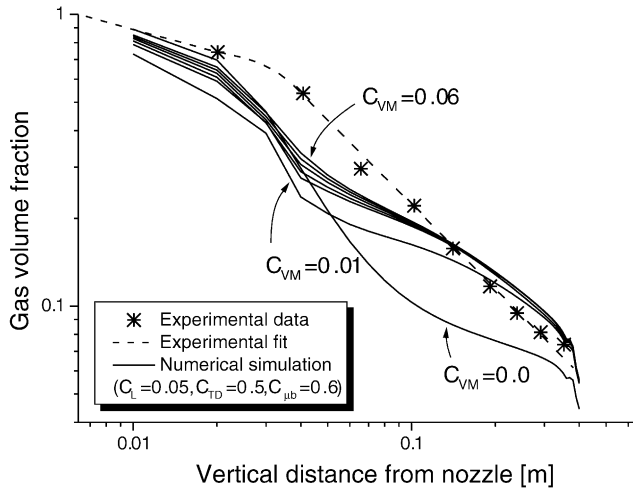
Fig. 5. Experimental [2] and numerical results for the gas fraction along the symmetry axis using different virtual mass coefficients and keeping constant all the others.

4.1. Drag force

In order to restrict the study to the non-drag forces, the same expression for the drag force is considered in all cases. Denoting the continuous phase by α and the dispersed phase by β, the total drag per unit volume in the continuous phase is usually written as

$$\boldsymbol{D}_{\alpha\beta} = c_{\alpha\beta}^{(d)}(\boldsymbol{U}_\beta - \boldsymbol{U}_\alpha), \tag{14}$$

where

$$c_{\alpha\beta}^{(d)} = \frac{3}{4}\frac{C_D}{d}r_\beta\rho_\alpha|\boldsymbol{U}_\beta - \boldsymbol{U}_\alpha|, \tag{15}$$

and d is the bubble diameter. For a particle of a given shape undergoing motion in a Newtonian incompressible fluid, C_D depends only on the Reynolds number

$$Re = \frac{\rho_\alpha U d}{\mu_\alpha}, \tag{16}$$

where μ_α is the molecular viscosity and ρ_α the density of the continuous phase, d the bubble diameter and $U = |U_\beta - U_\alpha|$. Dependence of the drag coefficient $C_D(Re)$ on the Reynolds number is given by the so called drag curve, which may be determined experimentally. One of the most used drag coefficients [6,7,10], although not completely realistic for bubbles, corresponds to the drag experimented by a rigid and isolated sphere, which is known as the standard drag curve. There are several empirical expressions for this curve, depending on the flow Reynolds number. One expression frequently used is Schiller and Nauman's [11]

$$C_D = \frac{24}{Re}(1 + 0.15 Re^{0.687}), \tag{17}$$

which is valid in the range $0 \leq Re \leq 1000$. This expression for C_D was used in this work.

4.2. Non-drag forces

4.2.1. Virtual mass

The virtual mass force accounts for the effect of the acceleration of the liquid displaced by the bubbles, and it can be modeled as

$$\boldsymbol{F}_\alpha^{VM} = r_\beta\rho_\alpha C_{VM}\left(\frac{D_\beta\boldsymbol{U}_\beta}{Dt} - \frac{D_\alpha\boldsymbol{U}_\alpha}{Dt}\right). \tag{18}$$

Operators $D_{\alpha,\beta}/Dt$ denote the material derivatives corresponding to each phase. The coefficient C_{VM} is equal to 0.5 for individual spherical particles [12]. For bubbles its value is much lower, and many times it is neglected [7,8]. In this study, considered values of C_{VM} are in the range 0–0.06.

Fig. 5 shows how the gas volume fraction changes when the virtual mass coefficient is varied. As expected, the inclusion of this force affects the gas volume fraction mainly in the region near the nozzle where the relative accelerations between phases are larger.

4.2.2. Lift

The lift force is given in terms of the slip velocity and the curl of the continuous phase velocity

$$\boldsymbol{F}_\alpha^L = r_\beta\rho_\alpha C_L(\boldsymbol{U}_\beta - \boldsymbol{U}_\alpha) \times (\nabla \times \boldsymbol{U}_\alpha). \tag{19}$$

The lift coefficient C_L is 0.5 for inviscid flow around a sphere [12], but it can take values as low as 0.01 for viscous flow.

Fig. 6 shows that variations of the lift coefficient affect the values of the volume fraction in the whole height of the bath. In addition, in a log–log graphic, the slope of the curve is modified.

Recent studies indicate that C_L depends on the Eötvös number, and it can take even negative values for large bubbles [13]. This is an important fact that should be taken into account if bubbles of different sizes are to be considered.
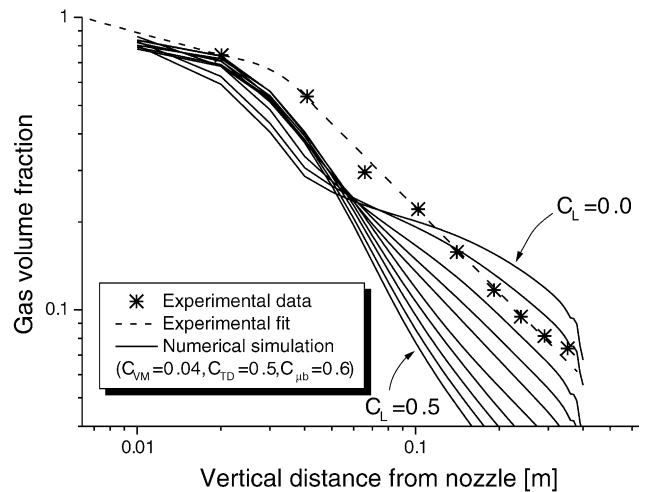

Fig. 6. Experimental [2] and numerical results for the gas fraction along the symmetry axis (same as Fig. 5). In this case only the lift coefficient is varied and all the others are kept constant.
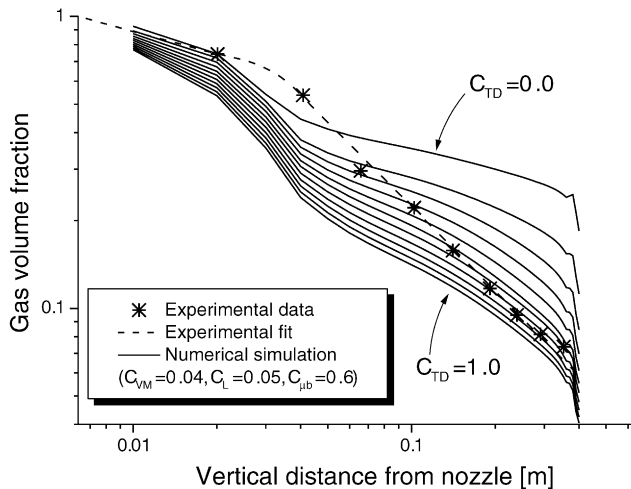
Fig. 7. Experimental [2] and numerical results for the gas fraction along the symmetry axis (same as Fig. 5). In this case only the turbulent dispersion force coefficient is varied and all the others are kept constant.

4.2.3. Turbulent dispersion force

This force appears as a consequence of the increment of diffusion due to turbulence. Since it is related to diffusion, it seems natural to incorporate this effect as a diffusive term in the continuity equation [7]. However, in this work this phenomenon was modelled as a force term in the moment equation [14], since in this way the contribution of diffusion to the velocity is included in the velocity variable.

The expression used for the turbulent dispersion force is [14]

$$\boldsymbol{F}_\alpha^{\mathrm{TD}} = -C_{\mathrm{TD}}\rho_\alpha k_\alpha \nabla r_\alpha, \tag{20}$$

where C_{TD} is a parameter that can be in the range 0.1–1.0 [9]. (For a recent discussion about modeling this force see Ref. [15].)

Fig. 7 shows that, like the lift force, when the turbulent dispersion force coefficient is changed, the gas volume fraction is modified over the whole height. It also shows that the slope of the curve does not change as much as when the lift force coefficient was varied.

4.3. Sato model

The Sato model takes into account the turbulence increment of the continuous phase induced by the dispersed phase. Denoting the continuous phase by α and the dispersed phase by β, the effective viscosity of the continuous phase is given by

$$\mu_{\alpha\,\mathrm{eff}} = \mu_{\alpha\,\mathrm{eff}} + \mu_{\mathrm{T}\alpha} + \mu_{\mathrm{T}\beta}. \tag{21}$$

The extra bubble induced turbulence term $\mu_{\mathrm{T}\beta}$ is modeled by

$$\mu_{\mathrm{T}\beta} = C_{\mu\mathrm{b}}\rho_\alpha r_\beta d|\boldsymbol{U}_\beta - \boldsymbol{U}_\alpha|, \tag{22}$$

where d is the bubble diameter, and $C_{\mu\mathrm{b}}$ is a constant usually equal to 0.6. The k and ε equations are solved only for the
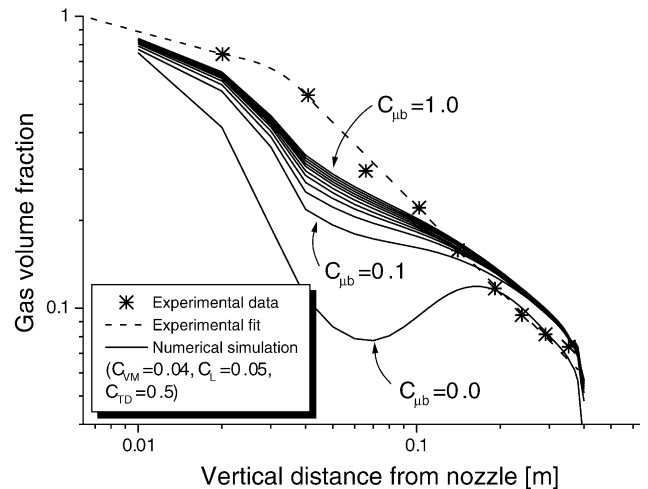

Fig. 8. Experimental [2] and numerical results for the gas fraction along the symmetry axis (same as Fig. 5). In this case only the Sato coefficient is varied and all the others are kept constant.

continuous phase, and the effective viscosity of the dispersed phase is given as

$$\mu_{\beta\,\mathrm{eff}} = \mu_{\alpha\,\mathrm{eff}}\frac{\rho_\beta}{\rho_\alpha}. \tag{23}$$

Fig. 8 shows the influence of this effect is mainly in the region near the nozzle, where the gas fraction and the relative velocity between the phases are greater.

4.4. Influence of bubble size

The more difficult region to be correctly described is the near nozzle region. There, bubbles are large and breakup and coalescence phenomena are important. As it was mentioned before, a good modeling of this effect is complicated, and since primary interest was on the region where the plume
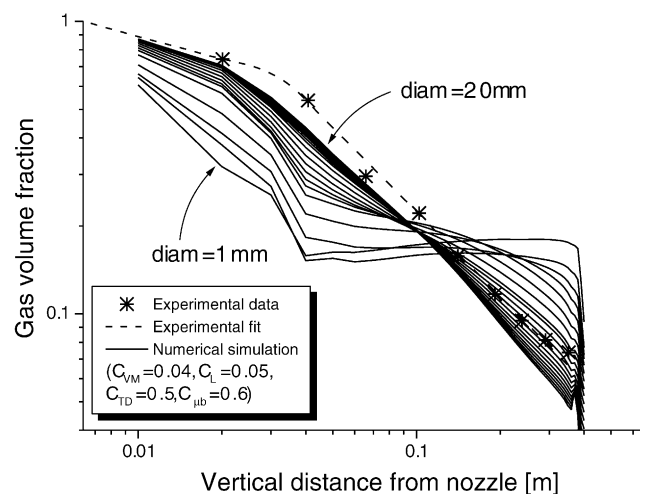

Fig. 9. Experimental [2] and numerical results for the gas fraction along the symmetry axis (same as Fig. 5). In this case only the bubble diameter is varied and all the other coefficients are kept constant.
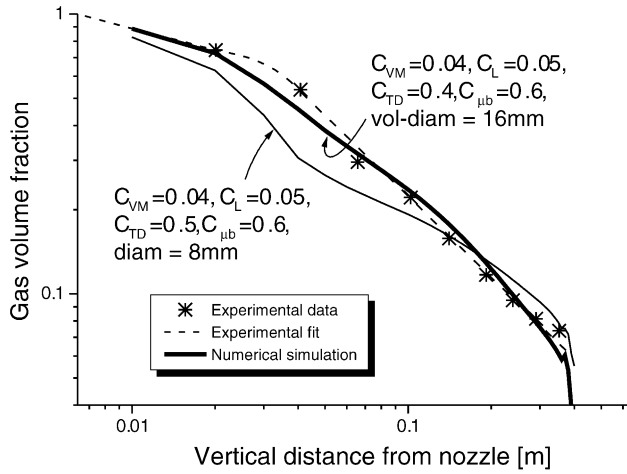
Fig. 10. Axial gas fraction with optimized numerical parameters compared with experimental data [2].
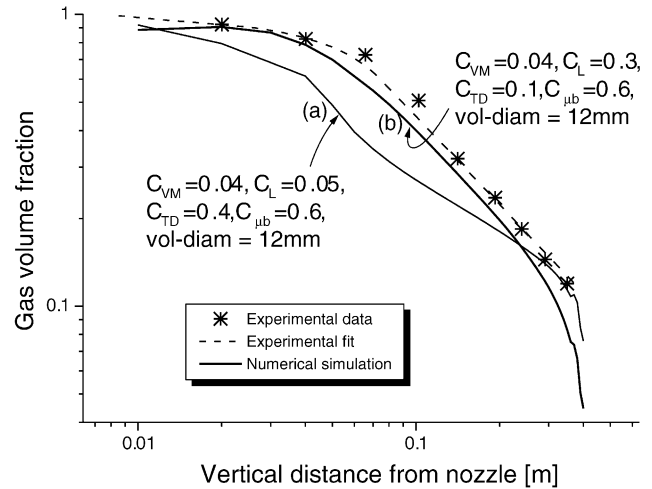

Fig. 11. Axial gas fraction with non-optimized (a) and optimized (b) numerical parameters compared with experimental data [2] for a case with a high gas flow rate.

is completely developed, just one bubble size was used to represent the gas.

Castillejos and Brimacombe [2] give the geometric mean diameter of the bubbles. This is the diameter used by Davidson [6], but in order to describe interphase forces, the volumetric mean diameter is usually used [12]. Still,

the volume-surface mean diameter (or the so-called Sauter mean diameter) [16] is also used in some cases because what appears in the derivation of the drag force is the quotient between the projected area and the volume of the bubble.
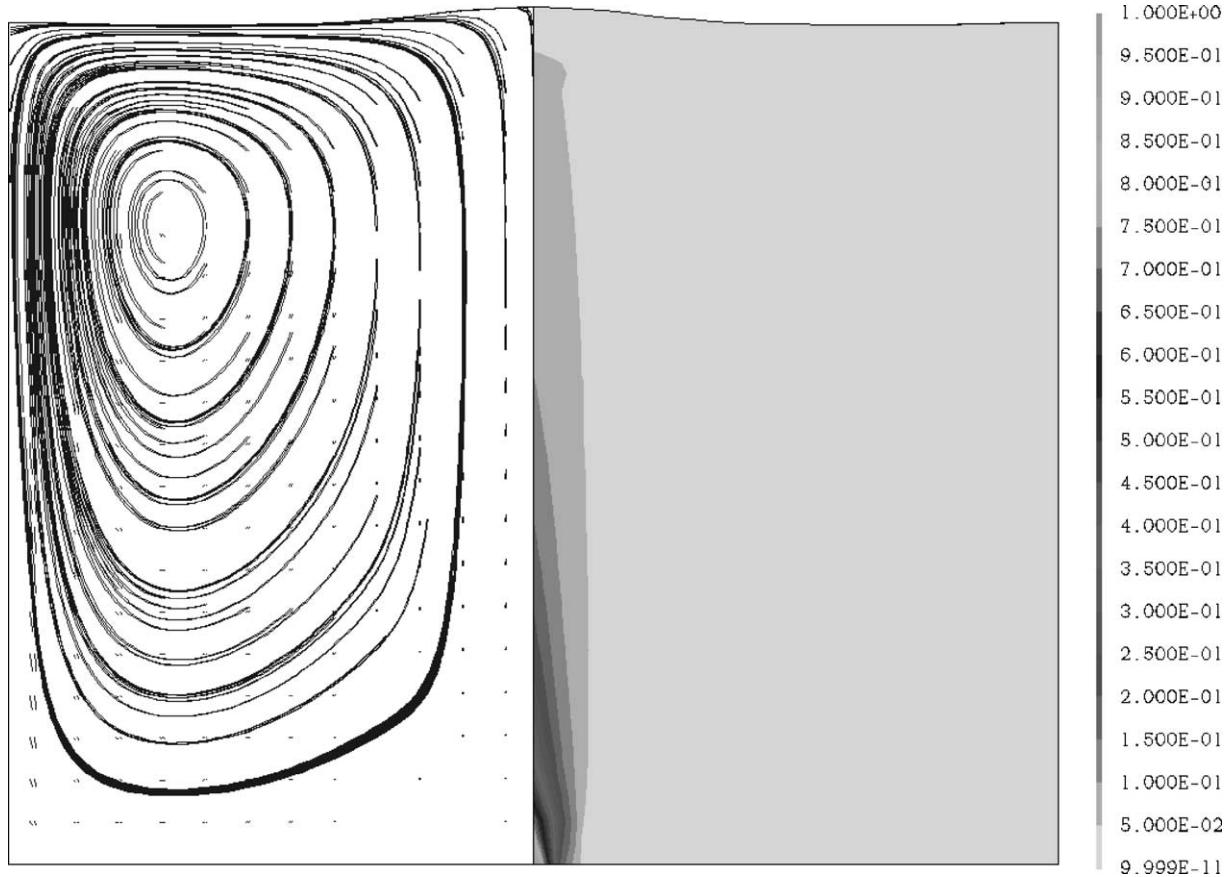

Fig. 12. Numerical results for the volume fraction of the air phase (right) and streak lines corresponding to the water phase (left) when the free surface is considered deformable.

Since there is no unified criteria about which diameter should be used to represent the bubble size distribution, the sensitivity of results to variations in diameter was analyzed. Fig. 9 shows how the volume fraction is modified when the diameter is varied, as well as the fact that when the same bubble size is adopted for all forces (drag and non-drag), results are better if the volumetric mean diameter is used. In this example, the volumetric mean diameter (16 mm) is twice the geometric mean diameter.

5. Analysis of different air–water plumes

After taking into account how the different parameters modify the numerical results, a better description of the system can be obtained. This is shown in Fig. 10 where preliminary (Fig. 4) and optimized results are compared.

From an experimental point of view, the system does not suffer substantial modifications in its behavior when the gas flow rate, the nozzle diameter or the bath depth are changed [2]. Therefore, good results are expected if the same coefficients for the non-drag forces are always used. Unfortunately, this is not the case. However, knowledge of the influence of the non-drag forces allows for a good description of the system in all cases, modifying only a few parameters. For example, Fig. 11 shows a case where the experimental conditions are the same as those in Fig. 4 but with a higher gas flow rate (1257 cm^3/s at STP). Curve (a) is the result of using the parameters of Fig. 10, and curve (b) was obtained

by modifying only the lift and the turbulent dispersion force coefficients.

6. Deformable free surface and three-phase system

In order to obtain a more realistic description of a metallurgical ladle, two more ingredients have to be included. One of them is the treatment of the free surface, and the other is the inclusion of the slag in the simulation.

Fig. 12 shows how the free surface is deformed. Results indicate that in the water–air system, the consideration of the deformation of the free surface does not substantially modify the solution, and a flat surface is a good approximation. In a graph like the one in Fig. 10, gas volume fractions with and without free surface are practically indistinguishable.

A water–air–kerosene system was simulated considering the kerosene as a third dispersed phase in the same way as the air. When the slag (kerosene) is included the velocity field in the water phase is substantially modified, as seen by comparing Fig. 2 to Fig. 13. Therefore, in order to make reasonable predictions about a real industrial ladle, the consideration of a three-phase system is essential.

7. Conclusions

The large influence of non-drag forces on the behavior of dispersed phases is shown in this work. Therefore, if the
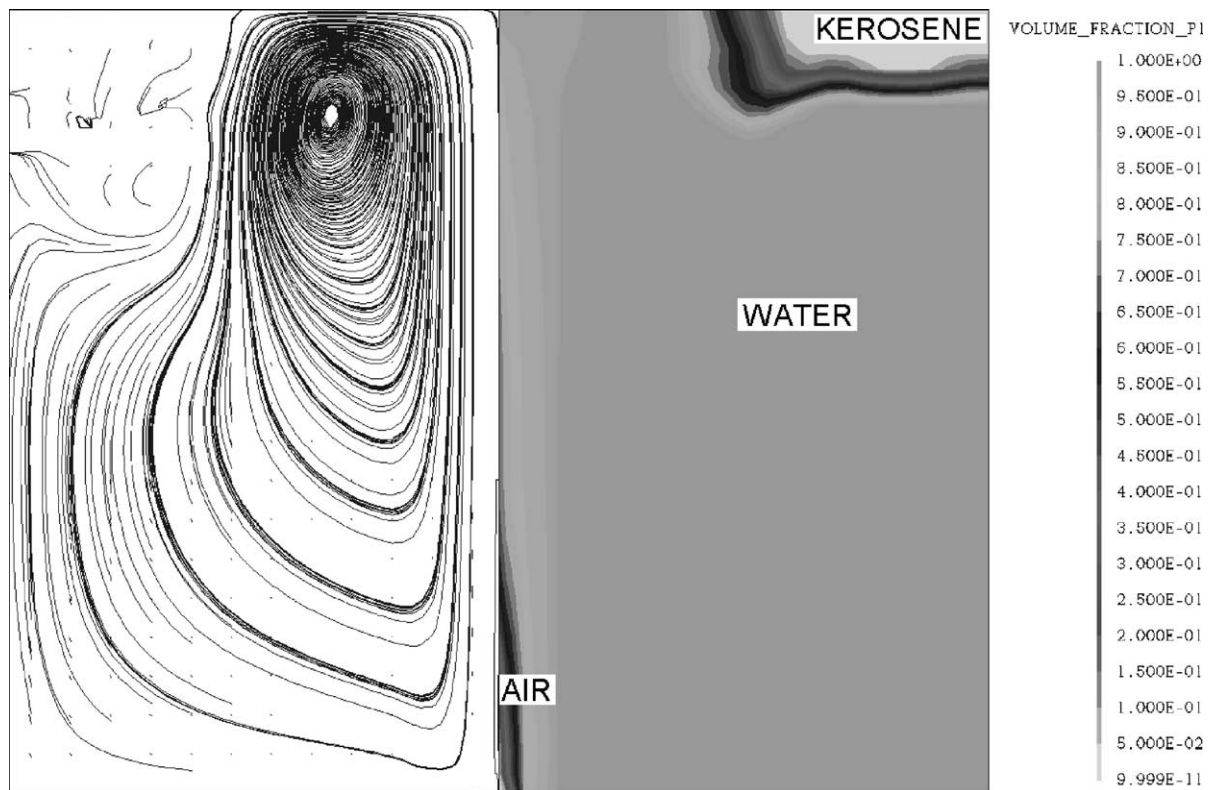

Fig. 13. Numerical results for the volume fraction (right) and streak lines corresponding to the water phase (left) when it coexists with kerosene and air phases.

interest is not only in the continuous phase motion, but also in a good description of the distribution of the dispersed phases (gas or slag), the effects produced by non-drag forces cannot be neglected.

In particular, a detailed analysis of the flow in a gas stirred ladle was made, with special emphasis in the behavior of gas fraction distribution. From this study it can be concluded that including non-drag effects, using a unique bubble size given by the volumetric mean diameter and adjusting a few parameters, the system can be correctly described in a wide variety of conditions.

The assumption of a flat free surface is a good approximation, and it proves to be reliable. On the other hand, preliminary results indicate that inclusion of the slag in the model drastically modifies the flow and therefore the consideration of a three-phase system (gas, molten metal, and slag) is mandatory to model a real industrial metallurgical ladle.

Acknowledgements

References

[1] D. Mazumdar, R.I.L. Guthrie, The physical and mathematical modelling of gas stirred ladle systems, ISIJ Int. 35 (1995) 1–20.

[2] A.H. Castillejos, J.K. Brimacombe, Measurement of physical characteristics of bubbles in gas–liquid plumes: Part II. Local properties of turbulent air–water plumes in vertically injected jets, Metall. Trans. 18B (1987) 659–671.

[3] M. Ishii, Thermo-Fluid Dynamic Theory of Two-Phase Flow, Eyrolles, Paris, 1975.

[4] D.C. Wilcox, Turbulence Modeling for CFD, second ed., DCW Industries Inc., La Cañada, CA, 1998.

[5] AEA Technology, User's Manual to CFX Version 4.4, AEA Technology plc, Harwell, UK (1998).

[6] M.R. Davidson, Numerical calculations of two-phase flow in a liquid bath with bottom gas injection: the central plume, Appl. Math. Modell. 14 (1990) 67–76.

[7] J. Hua, C.H. Wang, Numerical simulation of bubble-driven liquid flows, Chem. Eng. Sci. 55 (2000) 4159–4173.

[8] R.T. Lahey Jr., M. Lopez de Bertodano, O.C. Jones Jr., Phase distribution in complex geometry conduits, Nuclear Eng. Des. 141 (1993) 177–201.

[9] R.T. Lahey Jr., D.A. Drew, An analysis of two-phase flow and heat transfer using a multidimensional, multi-field, two-fluid computational fluid dynamics (CFD) model, Japan/US Seminar on Two-Phase Flow Dynamics, Santa Barbara, California, 2000.

[10] H. Turkoglu, B. Farouk, Numerical computations of fluid flow and heat transfer in a gas-stirred liquid bath, Metall. Trans. B 21B (1990) 771–781.

[11] L. Schiller, A. Nauman, A drag coefficient correlation, VDI Zeits. 77 (1933) 318–320.

[12] D.A. Drew, S.L. Passman, Theory of Multicomponent Fluids, Springer, 1998.

[13] A. Tomiyama, Struggle with computational bubble dynamics, Third International Conference on Multiphase Flow, ICMF'98, Lyon, France, 1998.

[14] M. Lopez de Bertodano, Turbulent Bubbly Two-Phase Flow in a Triangular Duct, Ph.D. thesis, Renssealaer Polytechnic Institute, Troy, New York, 1991.

[15] F.J. Moraga, A.E. Larreteguy, D.A. Drew, R.T. Lahey Jr., Assessment of turbulent dispersion models for bubbly flows in the low Stokes number limit, Int. J. Multiphase Flow 29 (2003) 655–673.

[16] R.S. Brodkey, The Phenomena of Fluid Motions, ubl. Co, Readin, MA, 1967.